An Analysis of Tsunami Sensitivity to Fault Plane Orientation Using a Rapid Linear Model

Nick Holschuh
Senior Integrative Exercise
March 9, 2011

Submitted in partial fulfillment of the requirements for a Bachelor of Arts degree from Carleton College, Northfield, MN.

Table of Contents

An Analysis of Tsunami Sensitivity to Fault Plane Orientation Using a Rapid Linear Model

Nicholas D. Holschuh
Carleton College
Senior Integrative Exercise
February 17, 2010

Advisors: Sarah Titus, Gerard Fryer

ABSTRACT

This study presents a comprehensive analysis of the effects of fault plane orientation and depth on tsunami hazard predictions using a linear mathematical model called "Rapid Inundation Forecasting for Tsunamis" (RIFT). Because it is possible to define earthquake fault characteristics with a high level of detail within RIFT, it is an ideal model for studying earthquake-tsunami dynamics. By incrementally changing fault strike, dip, rake, and hypocentral depth, it is possible to capture the effects of each source parameter on tsunami wave amplitude. I find that earthquake depth within 60 km of the seafloor has a negligible effect on tsunami wave heights. As fault dip varies within 15° of the plate interface orientation, the wave heights change by as much as 25% relative to the amplitudes predicted using décollement slip. Changing fault rake within 20° of pure thrust results in only a 10% change in tsunami amplitude, however if the motion on the fault is normal, amplitudes can differ from thrust generated waves by more than 50%. Fault strike is shown to control the direction of maximum energy propagation, causing local but large changes (up to 100%) in experienced wave heights. This study shows that assuming all tsunamigenic earthquakes occur on the plate interface can bias both global and local tsunami hazard predictions if the true source parameters deviate from the décollement orientation.

Keywords: Tsunamis; Geologic Hazards; Sensitivity Analysis; Focal Mechanism.

1. INTRODUCTION

Tsunamis pose both a societal and economic threat to coastal countries across the globe. The potential for devastation brought on by these long period waves is exemplified by the events of December 26, 2004, when a magnitude 9.3 earthquake occurred off the coast of Sumatra. More than 226,000 people were killed by the resulting tsunami, which exceeded a height of 9 meters along the coasts of the Indian ocean (Yeh, 2007). Given the human impact of these events, tsunamis have been a subject of great interest among natural scientists. From the Aleutian tsunami of 1946, which prompted the United States to develop a national tsunami warning system, through the Chile tsunami of 2010, geoscientists have been collecting and analyzing real time tsunami data in an effort to characterize the physical processes which control tsunami formation. Their ultimate goal has been to develop a mathematical framework which can explain tsunami generation, wave propagation, and coastal inundation.

Two criteria must be satisfied for a mathematical model to be useful during a real event: the model must be comprehensive enough to accurately predict tsunami hazard based on available (and often incomplete) information, and the model needs to be able to generate a prediction fast enough to be usable in emergency management procedures. There is a constant trade-off between these two qualities, as most efforts to reduce computation time necessitate simplifications to the calculation. Scientists have taken different approaches to reduce computational intensity, resulting in a wide variety of models. There are two distinct approaches that dominate the field: models which perform intensive computations before the event but in real time merely pull results from the database of pre-computed possibilities (e.g. Titov et al., 2001a), and those which perform

simplified calculations in real time but can include earthquake specific data in the computation (e.g. Wang et al., 2010).

Both of these methods for simplifying model computations have shortcomings; a systematic analysis of forecast results is required to understand the implications of a particular model simplification. There are two types of studies commonly conducted to characterize model performance. The first type of study consists of historic data comparison. These studies attempt to recreate observed wave heights from historic earthquakes, making it possible to determine whether or not there is any systematic error within the model (e.g. Wang, 2005; Greenslade, 2008; Lima, 2010). The second type of study looks at how model predictions vary with adjustments to model inputs. These sensitivity studies are especially important because the real time determination of earthquake depth and focal mechanisms is fraught with inaccuracy. Depending on teleseismic coverage, regional focal mechanisms can be calculated as quickly as minutes after earthquake rupture (Pasyanos et al., 1996), however the most accurate results cannot be determined for at least 2-12 hours after the earthquake (Helffrich, 1997). If a sensitivity study indicates that model results change dramatically with only slight differences in model input, very little confidence can be placed in model predictions generated within twelve hours of fault rupture.

Due to the relatively recent advent of real-time computer modeling, few tsunami sensitivity analyses have been conducted. Most tsunami literature is event-specific, and those studies that do look at tsunami model sensitivity in a more general sense only examine a narrow range of potential model inputs. This gap in the literature provides an obvious avenue for further study, however it limits the degree to which sensitivity study

results can be put in a larger context. The comprehensive sensitivity studies that have been performed look primarily at the effects of changing bathymetric and calculation grid resolutions (Grilli, 2010) or fault dimension and orientation (Titov et al., 2001b; Gica, 2007).

While sensitivity study results may be most valuable for specific model validation, these studies can also provide new insight on tsunami modeling and tsunamigenesis in general. Using RIFT ("Real-Time Inundation Forecasting of Tsunamis"), a rapid linear model developed at the Pacific Tsunami Warning Center (Wang et al., 2010), this study hopes to look more completely at the effects of fault plane location and orientation on tsunami dynamics.

2. RIFT BACKGROUND

From a geologic perspective, the source earthquake is the most important aspect of tsunamigenesis. RIFT is a particularly well-suited model for analyzing earthquake-tsunami dynamics, but to demonstrate why it is necessary to provide some mathematical and empirical background. This section will borrow heavily from the work of Wang et al. (2010) to explain the basics behind the mathematical framework of RIFT. The details omitted here can be found in the source paper, Okada (1985), and Synolakis (1991; 1993).

Tsunami calculation is commonly broken down into three distinct phases: wave generation, wave propagation, and wave inundation. Each phase is governed by a different set of physical equations, and depending on the desired level of sophistication, more or less complex analysis can be substituted in at any stage of the computation. Because tsunami models are designed with practicality in mind, the designers are forced

to balance this mathematical sophistication with ease of calculation. The governing philosophy of RIFT emphasizes the wave generation phase of calculation, ensuring complete customizability of the source earthquake. Wang et al. (2010) believe that earthquake fidelity is crucial to accurate tsunami modeling, and as a result they are willing to sacrifice complexity in wave propagation and inundation to allow for this source parameter customization.

2.1 RIFT Wave Generation

The wave generating process is modeled by estimating sea-floor deformation resulting from fault rupture. The Okada (1985) static displacement formula for rectangular faults is used to estimate sea-floor uplift, which determines the amount of water that is displaced. Within the model it is possible to provide specific values for a number of earthquake characteristics, including magnitude, hypocenter depth, fault strike, fault rake, fault dip, fault width, and fault length, Ideally fault orientation data will be available quickly enough for use during a real event; if not, RIFT is capable of estimating focal mechanisms in real time with only location data. After resolving the earthquake, the calculated water displacements act as the initial condition for the wave propagation calculations in the next phase of the model.

2.2 RIFT Wave Propagation

There is no analytical solution for the wave propagation equations; as a result the method for solving for wave motion involves discretizing the problem across the relevant ocean basin. The ocean is divided into individual cells, and the wave height in each cell is estimated recursively. The cell size is controlled within RIFT, and can range anywhere

from 15 arc-seconds up to 4 arc-minutes. As the resolution of this grid increases, prediction accuracy improves, but the computation time also increases.

Wave propagation within RIFT is based on the linear shallow water equations. These are defined as:

$$\boldsymbol{u}_{t+1} = \boldsymbol{u}_t - g\nabla\eta_t \tag{1}$$

$$\frac{\partial \eta_t}{\partial t} = -\nabla^a \cdot (\boldsymbol{u_t} h) \tag{2}$$

where $\boldsymbol{u_t}$ is a vector of lateral velocities, g is the vertical acceleration due to gravity, h is the ocean depth at rest, η is the sea surface height (as a deviation from the initial water depth h), and ∇ is the horizontal gradient operator. The a superscript signifies the value for an adjacent cell in the discretized grid, while the t subscript represents a discrete time period during wave propagation. Equation (1) is a solution of Newton's second law of motion, describing the wave propagation resulting from the initial water displacement. Equation (2) adds additional constraints to the surface displacement problem based on the law of conservation of momentum and vorticity.

The physical intuition behind the shallow water wave equations is not immediately obvious. Without any forces acting on the ocean, the sea surface will be flat (or spherical if looking on a whole Earth scale). The pressure at sea level (where $\eta_t = 0$) is assumed to be horizontally uniform, and equal to the ambient pressure applied on the sea surface by the atmosphere. When the sea-floor is deformed after an earthquake, the water column above the fault is either lifted up or dropped down. Because water is incompressible, if the fault rupture speed is fast enough, it is safe to assume that the sea surface displacement is equivalent to the seafloor displacement. The change in height of the water column results in an adjustment in pressure at the former ocean surface. The

pressure at the surrounding sea surface is still atmospheric pressure, resulting in a horizontal pressure gradient between the water over the fault and the water in the adjacent area. Gravity acts to restore the system to equilibrium, driving the horizontal motion of the wave described in equation (1), and illustrated in Figure 1. With a greater displacement of the sea surface, there is a higher lateral velocity for the wave.

Tsunami waves do not propagate in uniform concentric circles out from the source, like deep water waves do. This is because the long wavelength of tsunamis causes the wave to "feel-bottom" during the entire course of its propagation. If water wave orbitals interact with the sea-floor, propagation speed is directly controlled by water depth (h), according to the equation $V = \sqrt{gh}$. As the waves propagate over the non-uniform depth of the ocean with different speeds, the ocean ridges and coasts serve as a "wave guide", causing faster waves to bend towards the ridges and the coast line. As these waves bend in the open ocean, they converge and diverge from one another. This is the process governed by equation (2); the height of the sea surface at any given location is also a function of the wave height and velocity in an adjacent location during the previous time period.

Because there is very little energy dispersion over the course of wave propagation, the initial change of potential energy caused by sea-floor deformation stays in the system for a long period of time. To simplify calculation, RIFT assumes there is no energy lost at all during the relevant time period for hazard management. Although this is not the case, this assumption only leads to a slight overestimation of coastal wave heights. In reality, the wave continues to propagate through the global ocean basin until the energy has fully dissipated.

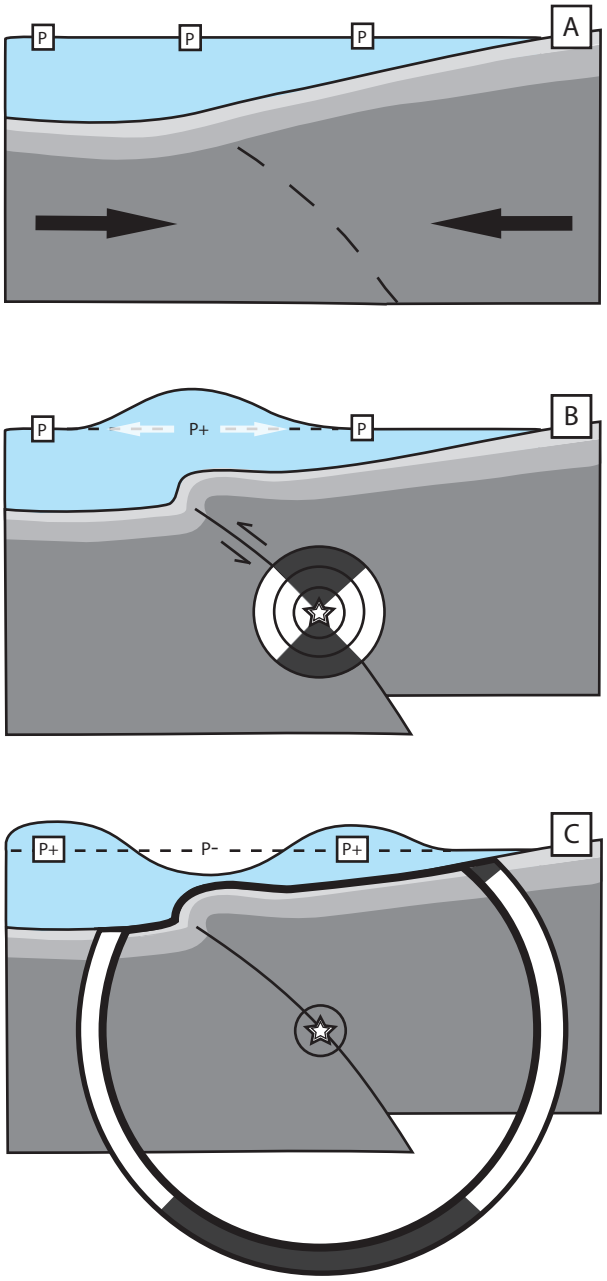

Figure 1. - Cartoon illustrating tsunamigenesis. Convergent plate motion results in the buildup of stress in the ocean crust. Image A illustrates the constant pressure state at the ocean's surface previous to the earthquake. During fault rupture (indicated in image B), compressional (black) and extensional (white) pressure waves are transmitted through the Earth's crust, allowing seismologists to calculate fault plane orientation when enough data arrives at seismic stations. The water above the fault is uplifted, resulting in a horizontal pressure gradient at the former ocean surface driving the tsunami waves. The water waves diverge from the area over the fault plane anywhere from 0.1 km/s to 0.25 km/s, while the seismic waves propagate away from the hypocenter at ~ 6 km/s (C).

2.3 RIFT Wave Inundation

Accurate inundation predictions require high resolution bathymetric data to calculate. Deep water wave propagation can be determined at relatively low resolutions, but the details of coastline bathymetry are lost if the calculation resolution is too low. As a result, there is a greater level of uncertainty for RIFT's coastal forecasts when compared to the deep ocean results. RIFT uses Green's law to calculate inundation values, a formula that characterizes the evolution of a wave's maximum amplitude until its breaking point (Synolakis, 1991). Green's law was selected over Boussinesq approximations, an alternate way of characterizing coastal wave interactions which incorporates energy dispersion and mathematical non-linearities, due to its ease of calculation. Boussinesq approximations will predict different results, however there is no apparent consensus in the field as to which type of approximation is the better choice (Synolakis and Skjelbreia, 1993).

3. SENSITIVITY ANALYSIS: JUSTIFICATION AND FRAMEWORK

RIFT lends itself to tsunami sensitivity analysis for many reasons, the first of which is its focus on the tsunami generation phase of calculation. Unlike other prominent tsunami models, for which earthquake sources are restricted to shallow thrusts along the décollement, within RIFT the user has control of fault length, width, rock shear modulus, earthquake magnitude, fault plane orientation, and depth. The high degree of specificity allows for a detailed analysis of the translation from earthquake to wave. Secondly, RIFT does not require tide gauge data to produce results. Many tsunami models are dependent on data inversion, fitting the raw model results to observed wave data in an effort to provide more reasonable wave amplitude estimates. The type of sensitivity analysis

conducted here is impractical for these uncalibrated models, given that their results are as dependent on incoming wave data as they are on initial earthquake conditions.

While RIFT's coastal inundation results have been empirically analyzed using historical observations (Fryer et al., 2010), the lack of detailed bathymetric data and the relatively low resolution used for calculation in this study (4 arc-minute grid) calls into question the accuracy of coastal results. Despite this added uncertainty to specific coastal prediction values, the general trends observed across different fault orientations should be correct. Because low resolution can bias near-field results more than those in the far-field, I examine more closely far-field coastal wave height estimates.

4. DATA

In this study, 151 modeled tsunamis are analyzed in an effort to quantify the marginal effects of changing earthquake fault parameters. All of the tsunamis are modeled around the same baseline earthquake, defined by the following characteristics: Longitude = 73°W, Latitude = 36°S, M_w = 8.5, Strike = 15°, Dip = 20°, Rake = 90°, Depth = 30 km. These values were chosen based on average values for the subducting Nazca plate west of Chile. The parameters that this study analyzes are fault strike, dip, rake, and hypocentral depth. For each model run, one variable is incrementally changed, making it possible to capture the resulting differences in tsunami wave characteristics due to a single parameter. This location, off of the west coast of Chile, was selected both for its recent earthquake activity and its use as a test location in the sensitivity analysis of the Cornell COMCOT model conducted by Gica et al. (2007). The wave propagation and inundation calculations are performed at a 4 arc-minute resolution across the entire Pacific Basin.

To quantify the effects of fault plane orientation, this study examines three different tsunami characteristics. The first tsunami quality discussed in each of the following subsections is the wave field. Using a series of maps, each of which was produced using deep ocean forecasts for a different set of source parameters, I compare the direction of propagation for the primary tsunami beam. This is largely qualitative, but provides valuable insight into both the local and global effects of changing source parameters.

The second tsunami characteristic discussed in each of the following subsections is the wave form. Wave form analysis is done by comparing the forecasted motion of a point particle over time, in an effort to quantify differences in wave characteristics. To help visualize differences in wave form, I have grouped the data into two different figure types. One is a plot of overlain time series, where each line represents the predicted wave height at the DMAR DART buoy location (shown in Figure 2) for a different set of source parameters. This makes it easy to compare wave attributes like wavelength, direction of first motion (whether or not the first tsunami indication is water receding or inundating the shore-face), and arrival time. The second set of Figures discussing wave form looks exclusively at maximum amplitudes for three central pacific locations: Rikitea Island, Easter Island, and the DMAR DART buoy (Figure 2).

The final tsunami characteristic discussed is coastal inundation. This is arguably the most important aspect of model prediction analysis, since hazard warning is based entirely on coastal amplitude predictions. I selected four important locations for hazard management during a Chilean tsunami (Valparaiso, Chile; Honolulu, HI; Los Angeles,

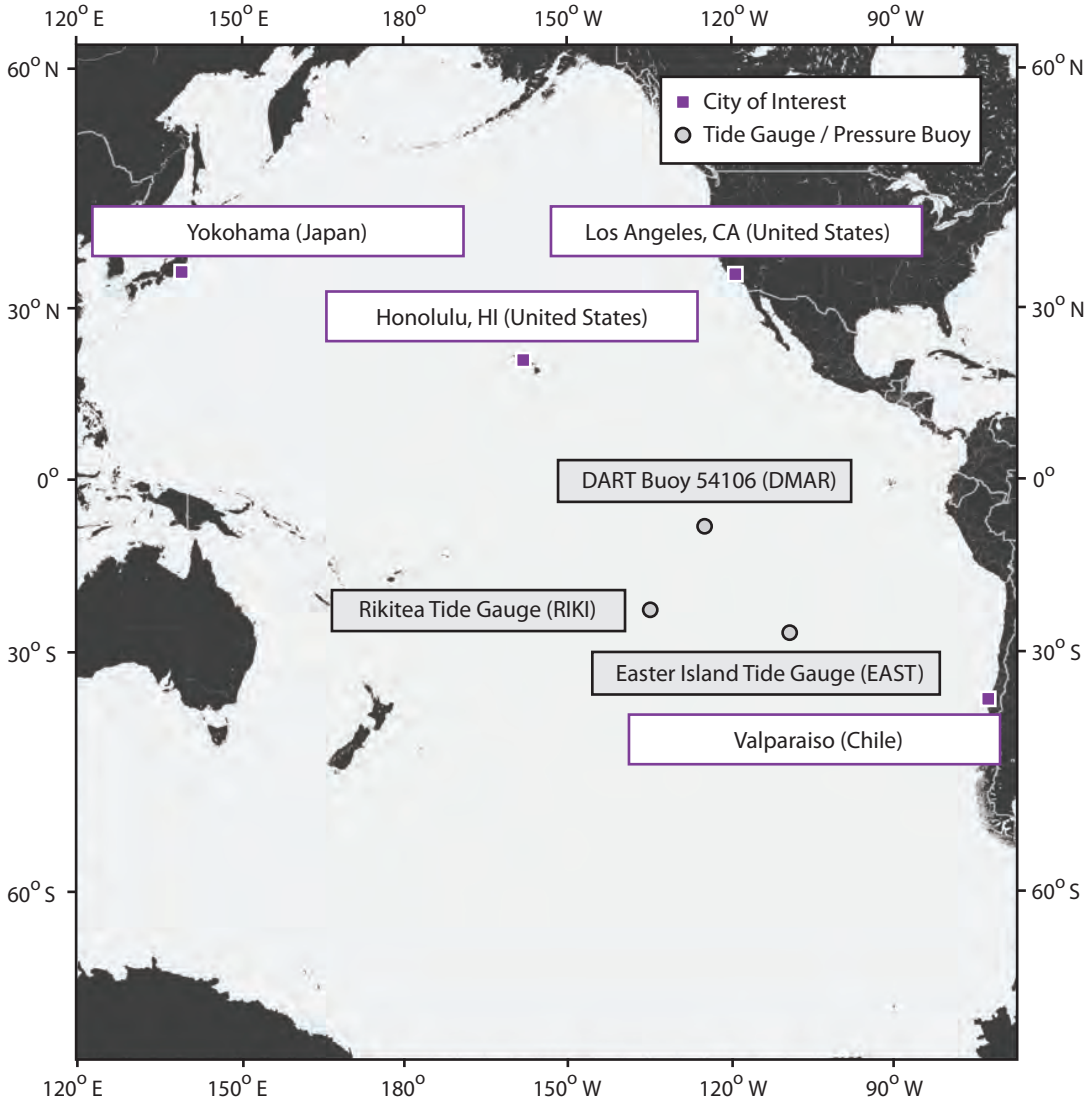

Figure 2. - Map indicating the locations of cities of interest (used for coastal inundation comparison), Tide Gauges (use to characterized the maximum and minimum experienced wave heights in different areas of the tsunami beam), and a DART Buoy (used for time series analysis).

CA; and Yokohama, Japan) to provide a representative sample of both near and far-field coastal wave height predictions.

4.1 Fault Strike

Strike values used for the sensitivity study ranged from 330° - 360°, and 000° - 060°. Each simulation incrementally adjusted the fault strike by 3°, resulting in a total of 31 generated tsunamis analyzed in this portion of the study.

The first and most significant characteristic I examine when studying the impact of fault strike on tsunamigenesis is the resulting wave fields. Figure 3 shows a series of maps produced using the model data, which indicate the maximum wave amplitudes experienced at each location in the open ocean. Note how the primary tsunami beam is oriented perpendicular to fault strike in all cases. As strike changes from 060° to 345°, the area of highest amplitude sweeps from north to south across the Pacific.

Figure 4 is a plot of the time series data that would be found at the DMAR DART buoy in the eastern Pacific. Together with Figure 5A, which illustrates the maximum and minimum wave heights found at each of the central Pacific sites, we can see that the maximum wave height experienced at DMAR occurs with a strike of 027°. Tsunami arrival in all cases is a positive wave (that is to say, water above mean ocean height), and in many cases the wave is not sinusoidal (Figure 4). Fault strike appears to drive local change in tsunami hazard, but not overall tsunami severity. RIKI experiences a maximum wave amplitude at a strike of 009°, while EAST experiences a maximum wave amplitude at a strike of 015°.

Figure 5B indicates the maximum experienced wave heights at each of 4 major cities around the Pacific. Valparaiso and Los Angeles show the strongest differences in

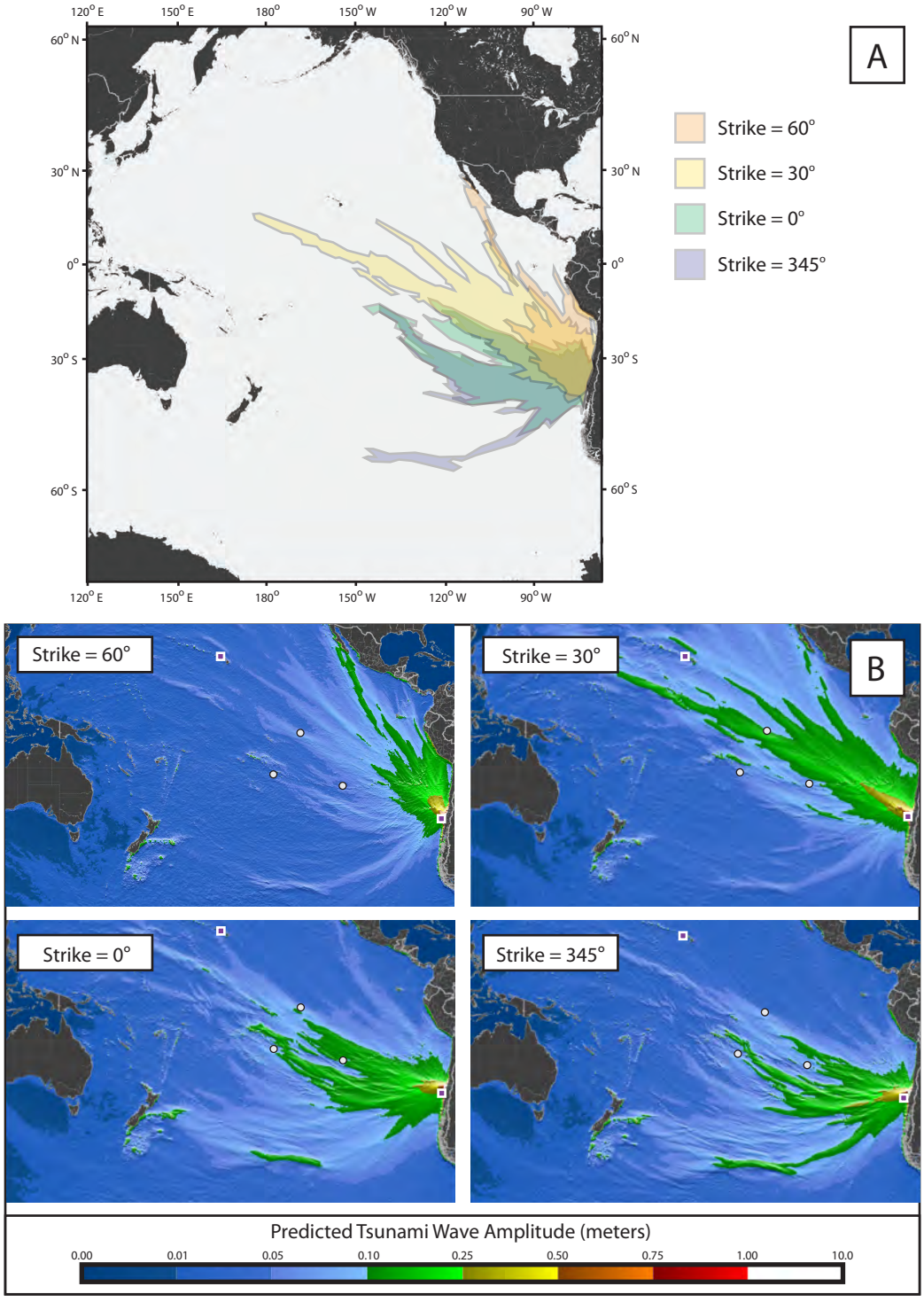

Figure 3. - Maps indicating the maximum predicted wave height in the open ocean for simulated tsunamis. Map A overlays the areas subjected to greater than 10 cm waves from each of the four sample tsunamis shown in part B. The goal is to illustrate the effect of earthquake strike on the beam of the resulting tsunami. Earthquake parameters other than strike are held constant at the following values: Depth = 30 km, Dip = 20°, Rake = 90°, M_W = 8.5, Latitude = 36° S, Longitude = 73° W.

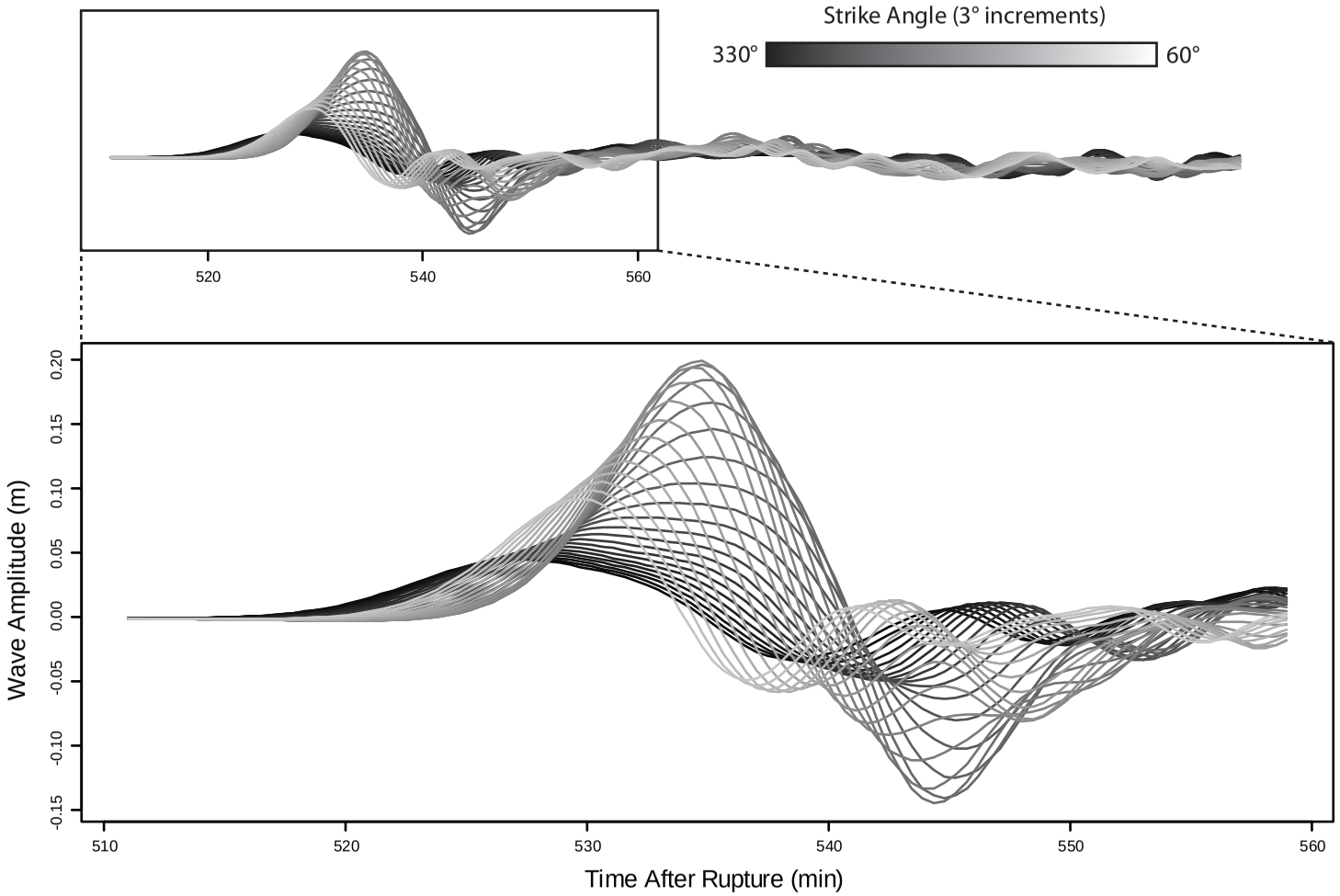

Figure 4. - Simulated time series data for dart buoy DMAR, illustrating the effect of fault plane strike on the resulting tsunami wave train. Each line represents a different simulation, with 40 in total. Earthquake parameters other than strike are held constant at the following values: Depth = 30 km , Dip = 20° , Rake = 90° , M_W = 8.5 , Latitude = 36° S , Longitude = 73° W.

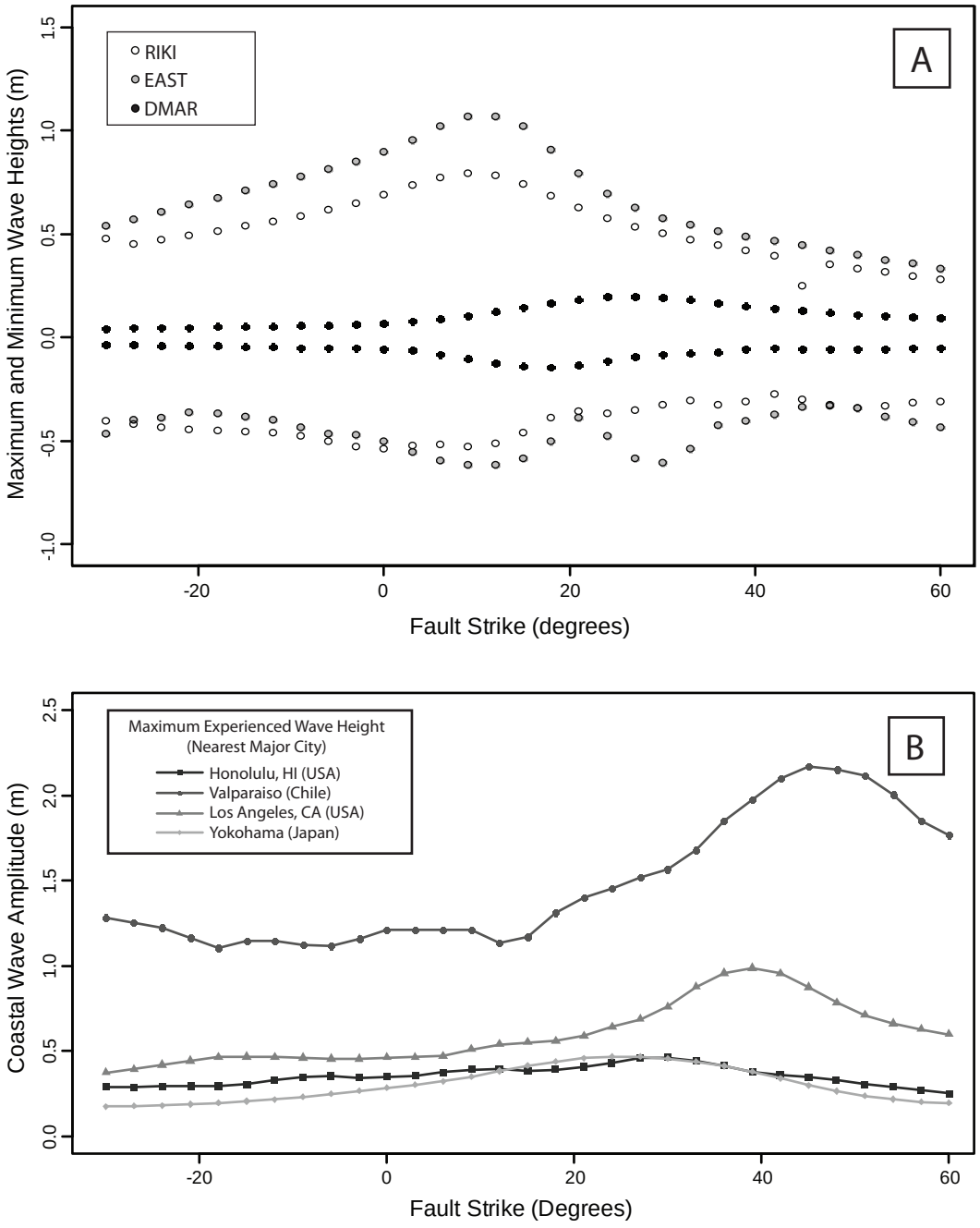

Figure 5. - Graph A illustrates the maximum and minimum wave heights experienced at tide gauges EAST, RIKI, and DART buoy DMAR. Tsunami parameters other than strike are held constant at the following values: Depth = 30 km, Dip = 20°, Rake = 90°, M_W = 8.5, Latitude = 36° S, Longitude = 73° W. Graph B is a plot of coastal wave heigh estimates for varying strike. Estimates calculated using Green's Law.

experienced wave heights as a result of a change in strike. Both of these locations are north of the source, and as is expected from the wave field analysis, energy is directed toward them when the fault strikes roughly East-West. Honolulu and Yokohama show highest experienced wave height in the 20°-30° strike range, although the difference across all strikes is only ~0.3 m.

4.2 Fault Dip

To capture the effects of fault dip, tsunamis were modeled with fault dip angles ranging from 2° to 90°. Each model run was performed with a 2° change in fault dip, resulting in 45 total modeled tsunamis.

Figure 6 shows a selection of maps of forecasted open ocean tsunami wave heights using different fault dips. There are two things to note on these maps. The first important feature is the presence of a secondary tsunami beam, which appears roughly North-South for steeper fault planes. Tsunami energy is focused perpendicular to strike for those earthquakes with fault planes dipping less than 20°, but as dip angle increases, more wave energy is directed parallel to fault strike. This appears clearly in the South Pacific, with wave heights east of New Zealand noticeably higher with higher fault dip.

The wave trains illustrated in Figure 7 indicate that wave amplitude differences at DMAR resulting from different dip angles are negligible. What is significant in this plot is the nature of the wave first arrival. As dip increases, the first wave signal becomes increasingly negative. As a result, the arrival of the first wave crest varies by almost 20 minutes from shallow dipping faults to steeply dipping faults. Figure 8A shows that maximum wave heights have a range of about half of a meter for the RIKI and EAST tide gauges. The highest possible waves occur when the fault dips ~60°.

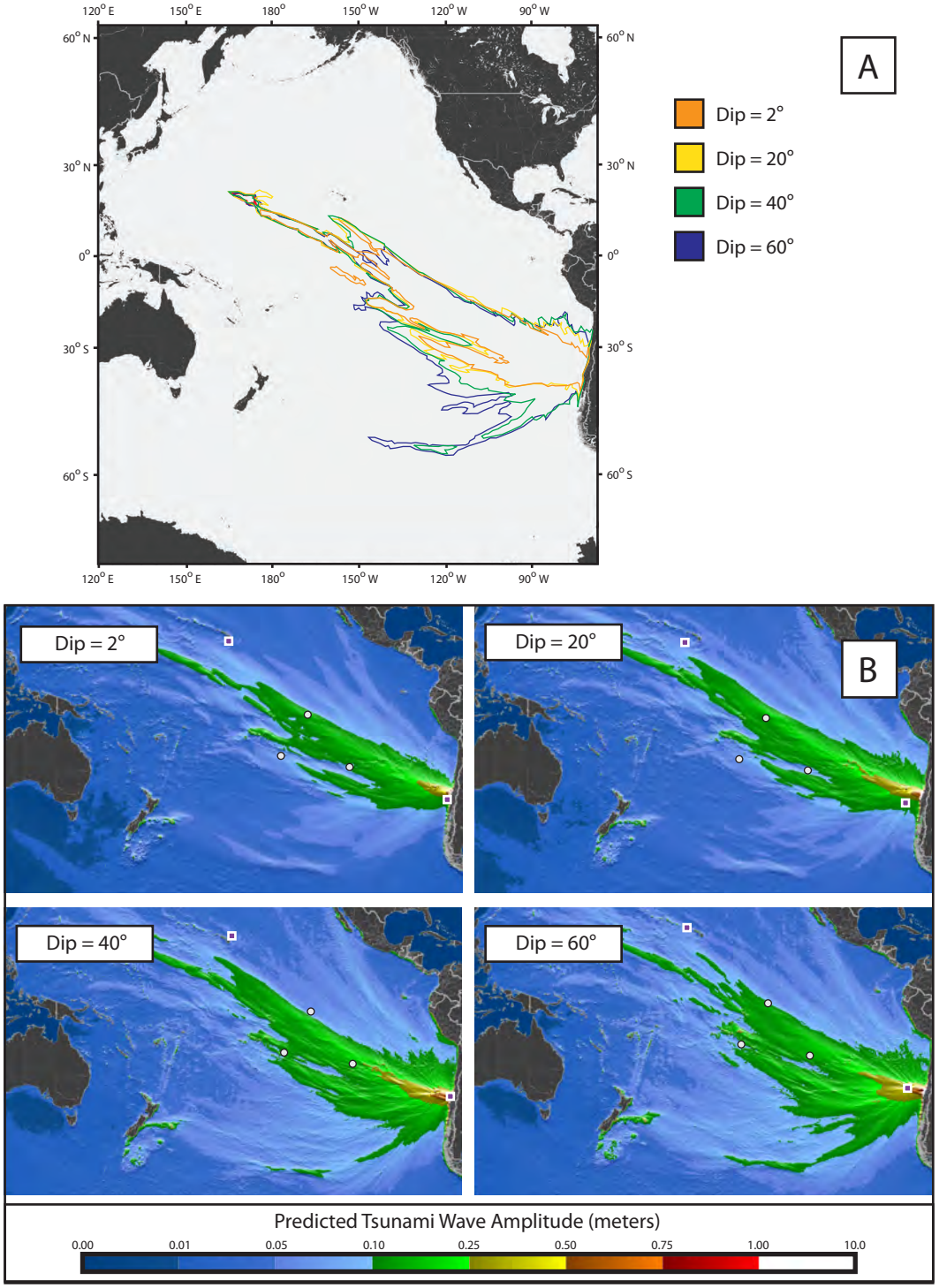

Figure 6. - Maps indicating the maximum predicted wave height in the open ocean for simulated tsunamis. Map A overlays the areas subjected to greater than 10 cm waves from each of the four sample tsunamis shown in section B. The goal is to illustrate the effect of earthquake dip on the beam of the resulting tsunami. Earthquake parameters other than dip are held constant at the following values: Depth = 30 km, Strike = 15°, Rake = 90°, M_W = 8.5, Latitude = 36° S, Longitude = 73° W.

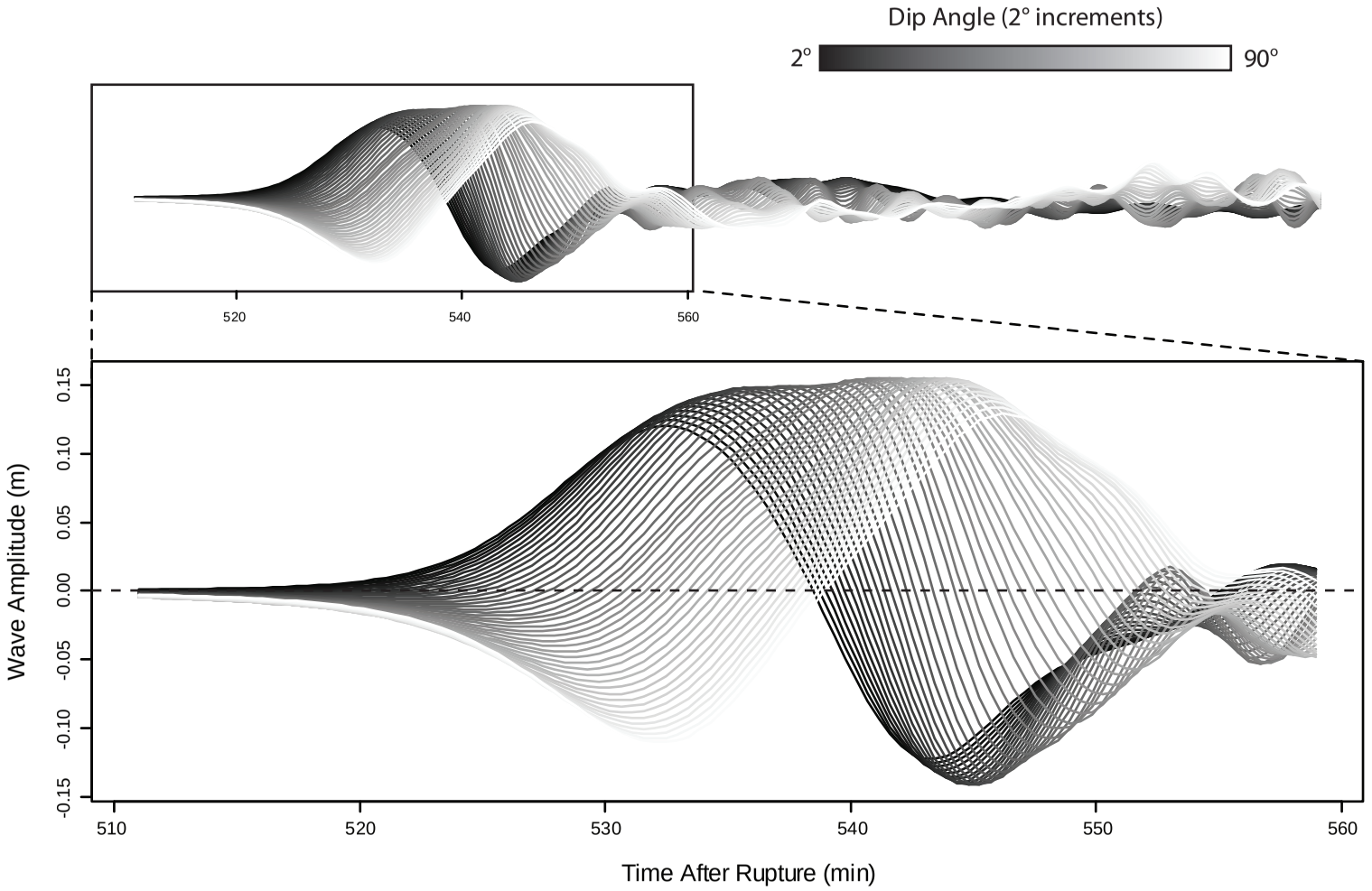

Figure 7. - Simulated time series data for dart buoy DMAR, illustrating the effect of fault plane dip on the resulting tsunami wave train. Each line represents a different simulation, with 40 in total. Earthquake parameters other than dip are held constant at the following values: Depth = 30 km, Strike = 15°, Rake = 90°, M_W = 8.5, Latitude = 36° S, Longitude = 73° W.

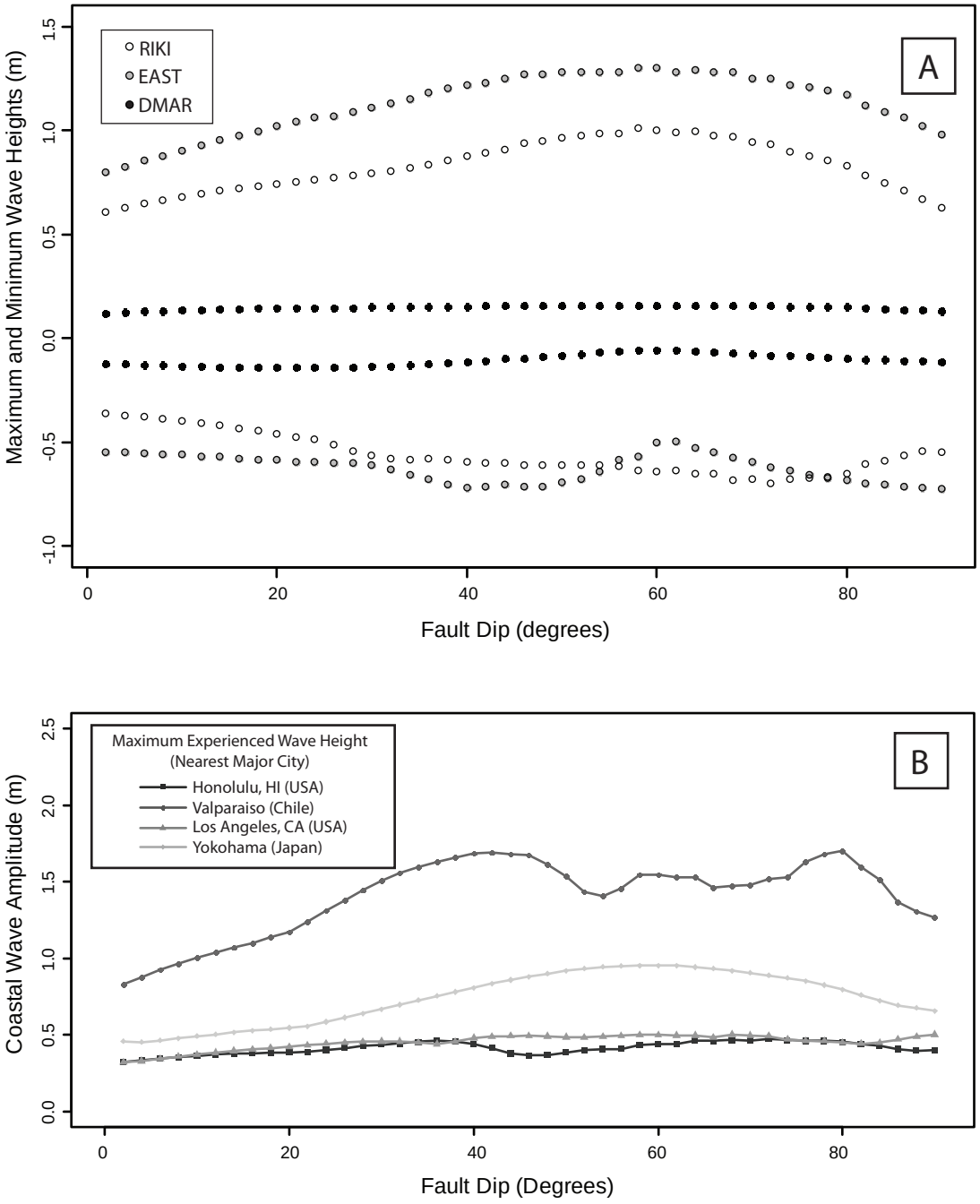

Figure 8. - Graph A illustrates the maximum and minimum wave heights experienced at tide gauges EAST, RIKI, and DART buoy DMAR. Earthquake parameters other than dip are held constant at the following values: Depth = 30 km, Strike = 15°, Rake = 90°, M_W = 8.5, Latitude = 36° S, Longitude = 73° W. Graph B shows the predicted coastal wave heights as dip varies. Estimates are calculated using Green's Law.

The maximum coastal wave heights plotted in Figure 8B corroborate many of the trends indicated by the other data sets. Valparaiso and Los Angeles experience noticeably higher coastal forecasts for dips >30°. Japan and Hawaii do not appear to experience substantial variation in their coastal wave forecasts.

4.3 Fault Rake

To analyze the effects of rake on tsunamigenesis, 40 tsunamis were modeled with rakes ranging from -180° to 180°. Right-lateral strike slip faults correspond to a rake of -180°/180°, normal faults have a rake of -90°, left-lateral faults have a rake of 0°, and reverse faults have a rake of 90°. Both strike-slip and dip-slip fault configurations are examined, although strike slip-faults are generally incapable of generating tsunamis. The only case where lateral water displacement can result in wave generation is when the horizontal motion drives water up slope.

As the source transitions from dip-slip to strike-slip motion, there is a clear change in the resulting tsunami wave field. Strike-slip motion generates almost no wave, which is expected. As indicated by the maps in Figure 9, the pure normal fault configuration generates the greatest total tsunami threat, but both pure dip-slip configurations create comparable wave fields.

Figures 10 and 11A indicate that the two types of dip-slip faults produce inverse wave forms. The difference can be clearly seen in the data for Easter Island; perfectly normal motion produces a maximum of roughly 0.5 m and a minimum of -1 m, while reverse faults generate a maximum of 1 m and a minimum of -0.5 m. In the time series data from DMAR, the maximum positive and negative wave heights are roughly equivalent for all rakes (about 15 cm for both a normal and reverse fault). This is not the

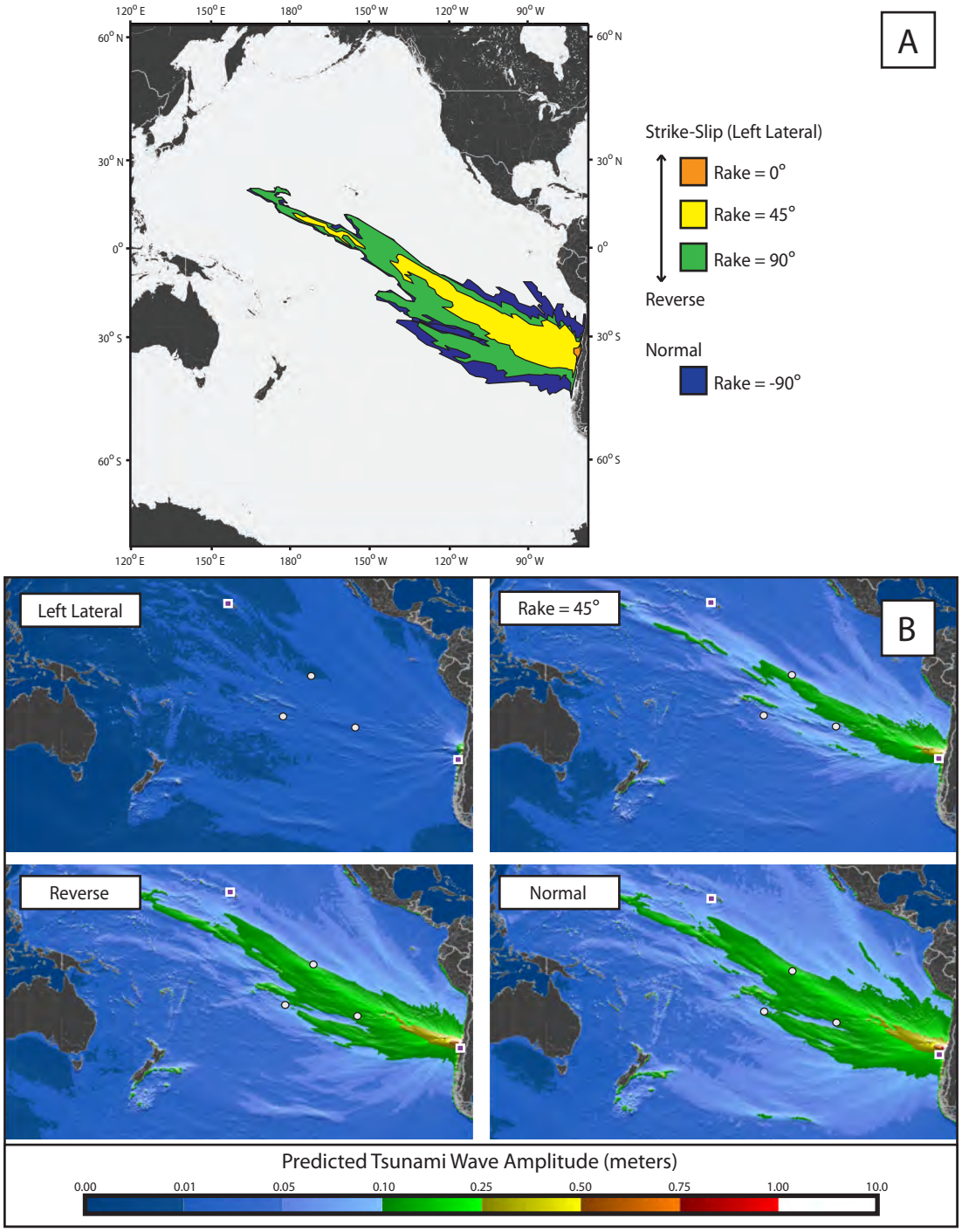

Figure 9. - Maps indicating the maximum predicted wave height in the open ocean for simulated tsunamis. Map A overlays the areas subjected to greater than 10 cm waves from each of the three sample tsunamis in section B. The goal is to illustrate the effect of earthquake rake on the beam of the resulting tsunami. Earthquake parameters other than rake are held constant at the following values: Depth = 30 km, Strike = 15°, Dip = 20°, M_W = 8.5, Latitude = 36°S, Longitude = 73° W.

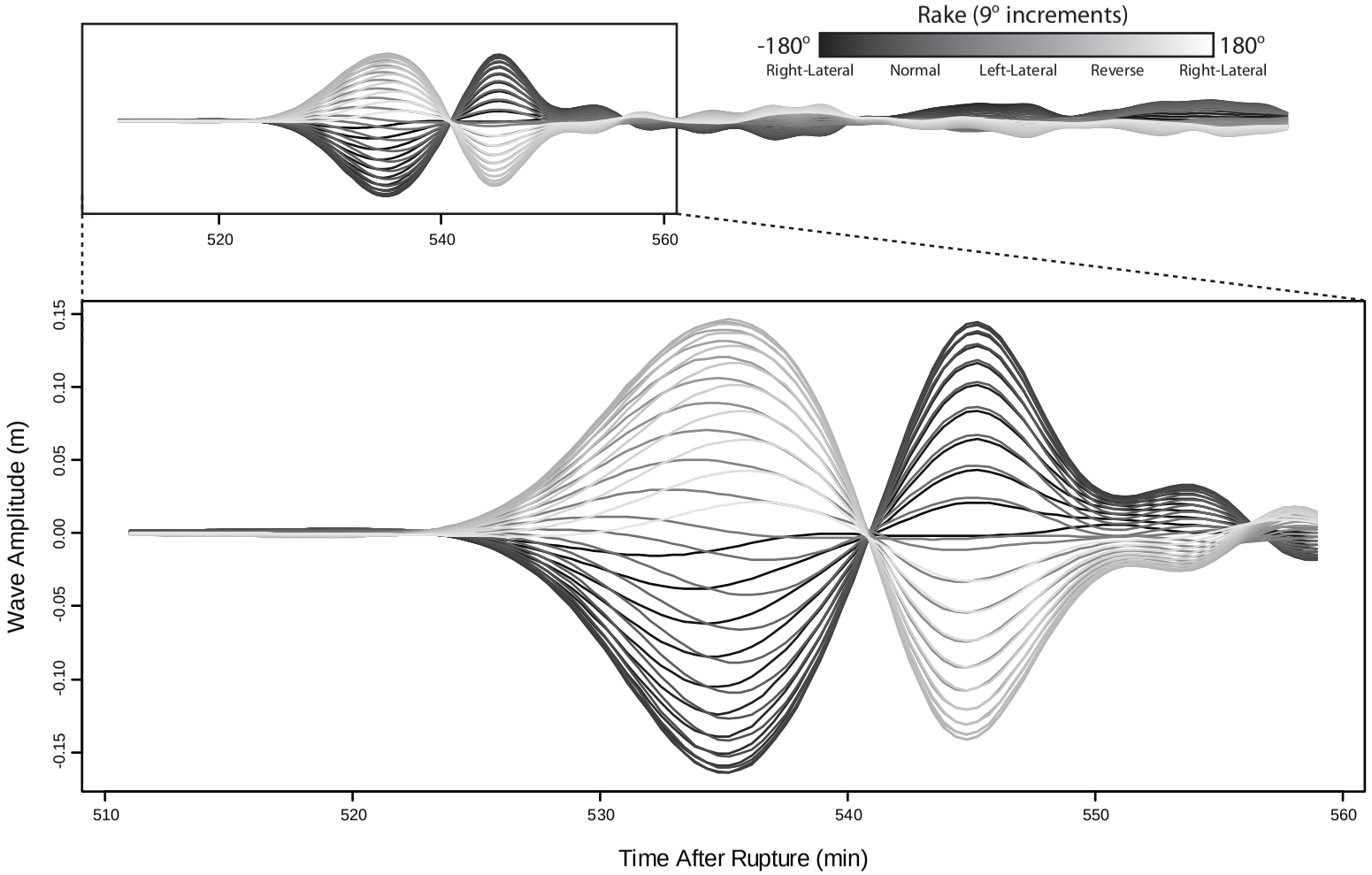

Figure 10. - Simulated time series data for dart buoy DMAR, illustrating the effect of fault rake on the resulting tsunami wave train. Each line represents a different simulation, with 40 in total. Earthquake parameters other than rake are held constant at the following values: Depth = 30 km, Strike = 15°, Dip = 20°, M_W = 8.5, Latitude = 36°S, Longitude = 73°W.

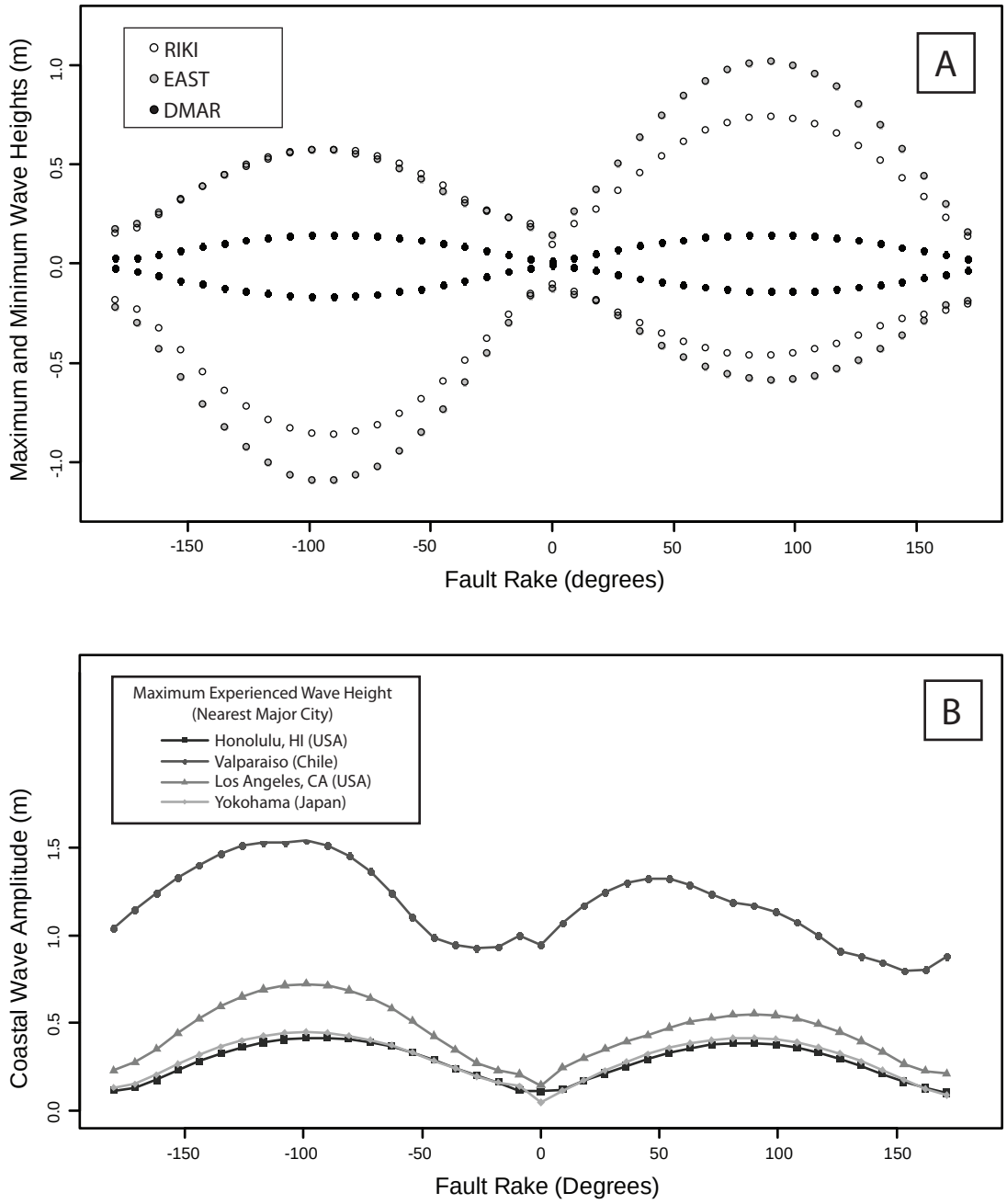

Figure 11. - Graph A illustrates maximum and minimum wave heights experienced at tide gauges EAST, RIKI, and DART buoy DMAR. Earthquake parameters other than rake are held constant at the following values: Depth = 30 km, Strike = 15°, Dip = 20°, M_W = 8.5, Latitude = 36° S, Longitude = 73° W. Graph B shows coastal wave height estimates as rake is incrementally changed. Values calculated using Green's Law.

case for EAST and RIKI, which indicate a clear asymmetry between the positive and negative waves experienced. They show that, for these locations, reverse faults will produce wave heights of 75 cm and 100 cm respectively. For EAST, this is a 2-fold increase over the maximum wave created from a normal fault rupture.

Because the first motion of a tsunami created by a normal fault is a negative wave (the darker lines in Figure 10), there is more time between fault rupture and the arrival of the first wave crest for normal faults than there is for reverse faults (the lighter lines in Figure 10). That difference is on the order of 10 minutes.

Figure 11B shows the maximum experienced coastal wave heights as the earthquake rake varies. Notice for the two possible strike slip faults (-180°/180° and 0°) there is almost no detectable tsunami in the far-field. Wave amplitudes are also significantly lower in the near field (Valparaiso) for strike slip faults as compared to those generated by dip slip earthquakes. The higher maximum wave amplitudes for Los Angeles and Valparaiso were caused by normal faulting, which is what is expected from the wave field analysis, but is unexpected when compared to the time series data in Figure 11A.

4.4 Hypocentral Depth

The final parameter that I examined is hypocenter depth. Hypocenter depths range from 18 km – 57 km, with an incremental increase of 1 km for each model run, resulting in a total of 40 simulations. It is important to note, however, that because RIFT estimates the area of fault plane rupture based on earthquake magnitude, there are restrictions on how shallow an earthquake can be for any given magnitude. The dipping plane needs to be a certain size, and for an M_w of 8.5 and a dip of 20°, RIFT requires 17 km of rock

above the focus to allow for a big enough rupture area within the sea-floor. This restricts the minimum possible hypocenter depth given this dip and magnitude to 18 km.

There is almost no perceptible difference in the wave field as depth increases. The maps in Figures 12 and 13 indicate only a slight reduction to wave heights in the near field (most apparent in the areas experiencing between 0.25 m and 0.5 m). By a depth of 56 km, there is a notable reduction in the ocean basin area experiencing >10 cm wave heights, but the wave height change with each incremental addition to depth is negligible.

Figure 14 shows the simulated time series data at DMAR, and illustrates the relative impacts of different depths on the wave form of the resulting tsunami wave train. Amplitude is maximized around a depth of 25 km, although the range of peak amplitudes across all depths is less than 5 cm. Figure 15A illustrates the maxima and minima for water level heights, indicating just how little variability there is across this range of hypocentral depths. There is a negative correlation found between depth and tsunami wave heights for depths greater than 25 km, but in the range 25 km – 57 km this negative relationship results in very little actual change in the experienced wave heights.

The coastal hazard data plotted in Figure 15B serves to reinforce the conclusion drawn from the other data sets: depth has almost no effect on tsunami wave hazard. The only effect that is visible is a negative correlation between depth and maximum wave amplitude. This is pronounced at all depths for the near field location, however it is only seen at depths greater than 26km for far-field locations.

5. DISCUSSION

While we know that water displaced by movement of the ocean floor is what drives most tsunamigenesis (Comer, 1984), the impact of specific fault geometry on the resulting tsunami is less well understood (Okal, 2009). Tsunami warning centers are often

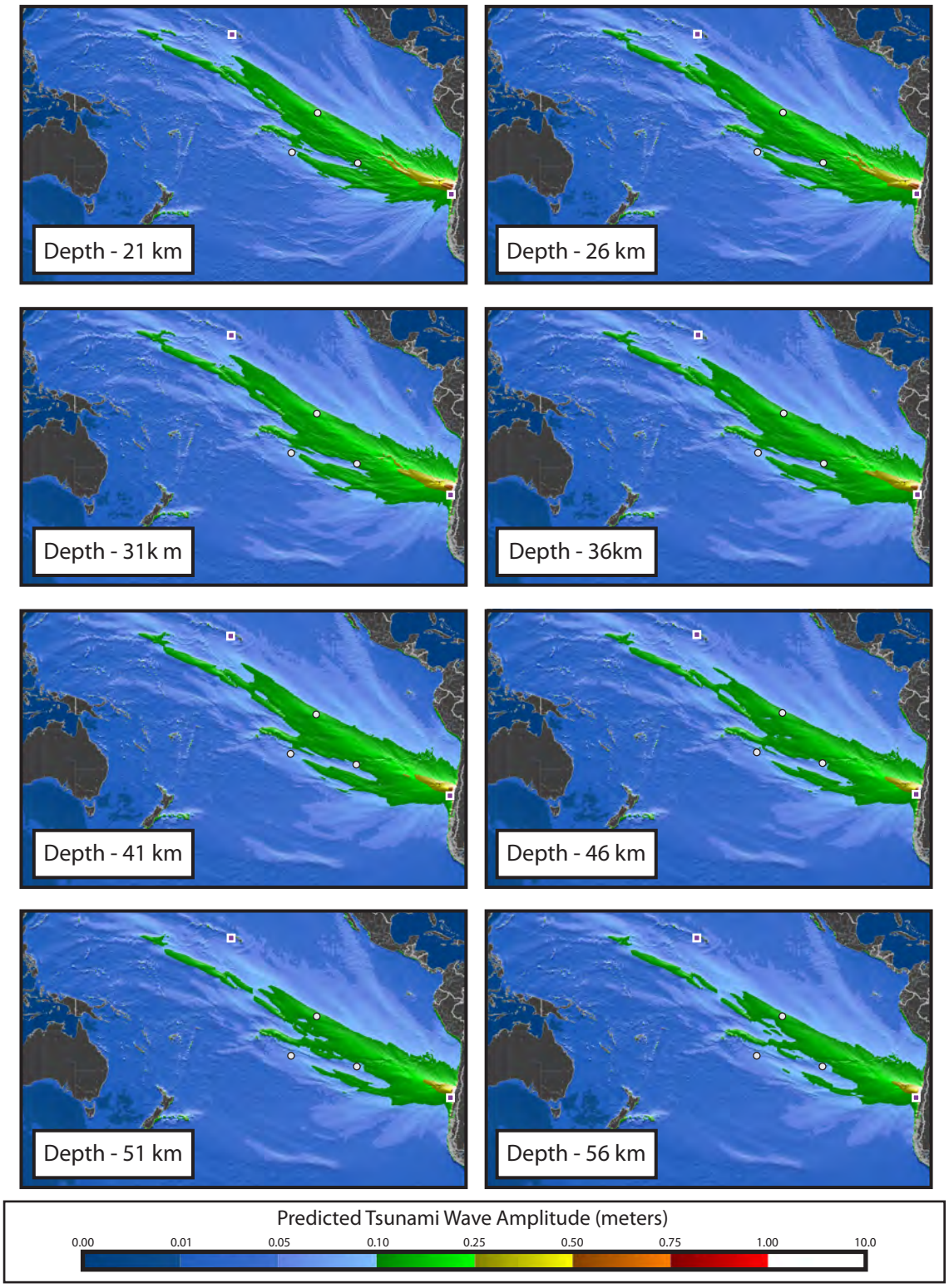

Figure 12. - Maps indicating the maximum predicted wave height in the open ocean for simulated tsunamis. Earthquake parameters other than dip are held constant at the following values: Depth = 30 km, Strike = 15°, Dip= 20°, M_W = 8.5, Latitude = 36° S, Longitude = 73° W.

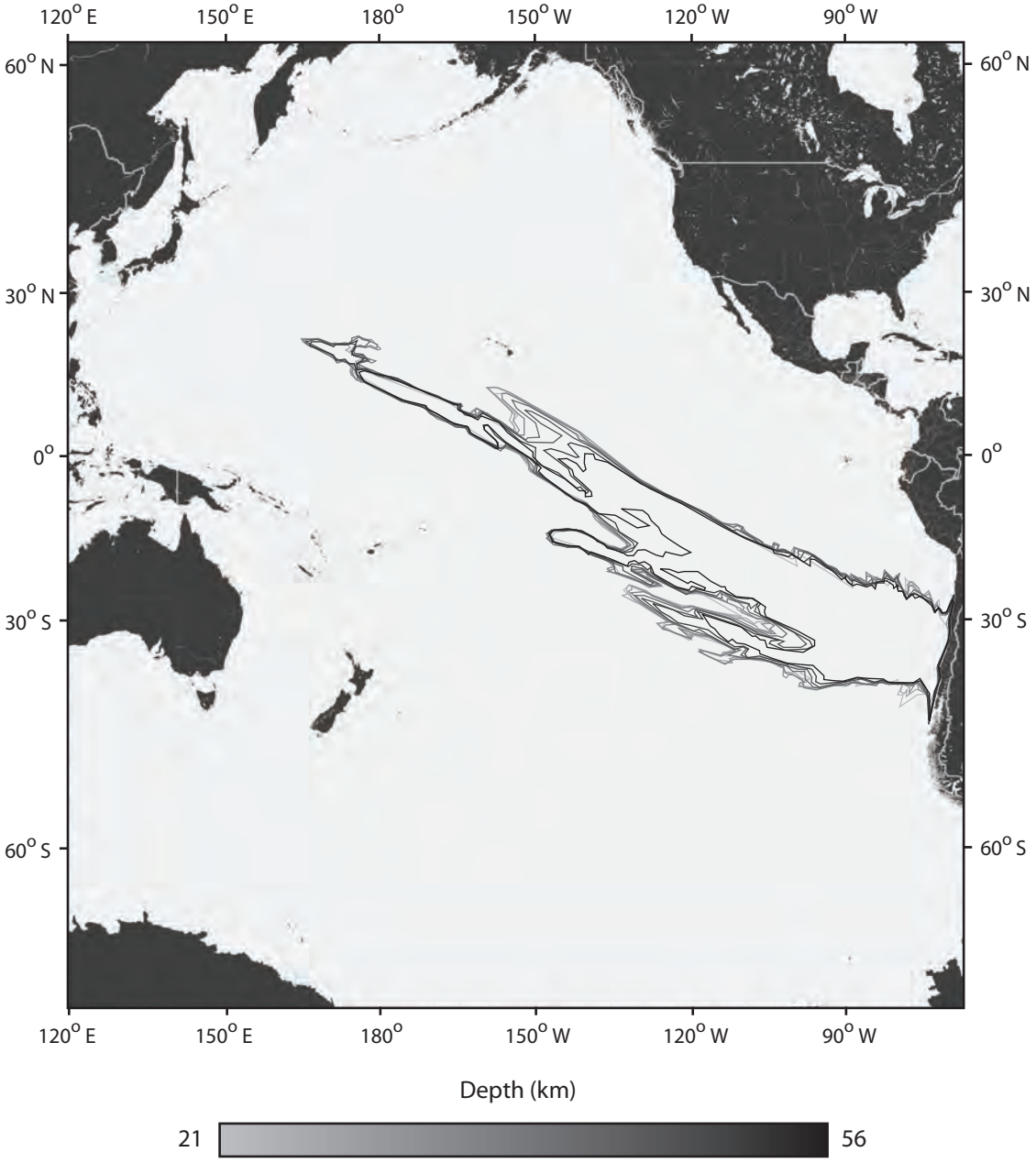

Figure 13. - Map overlaying the areas of 10 cm or greater waves as hypocentral depth is adjusted. Each new wave field outline represents a 5 km increase to hypocenter depth. Note how little variability there is across depths.

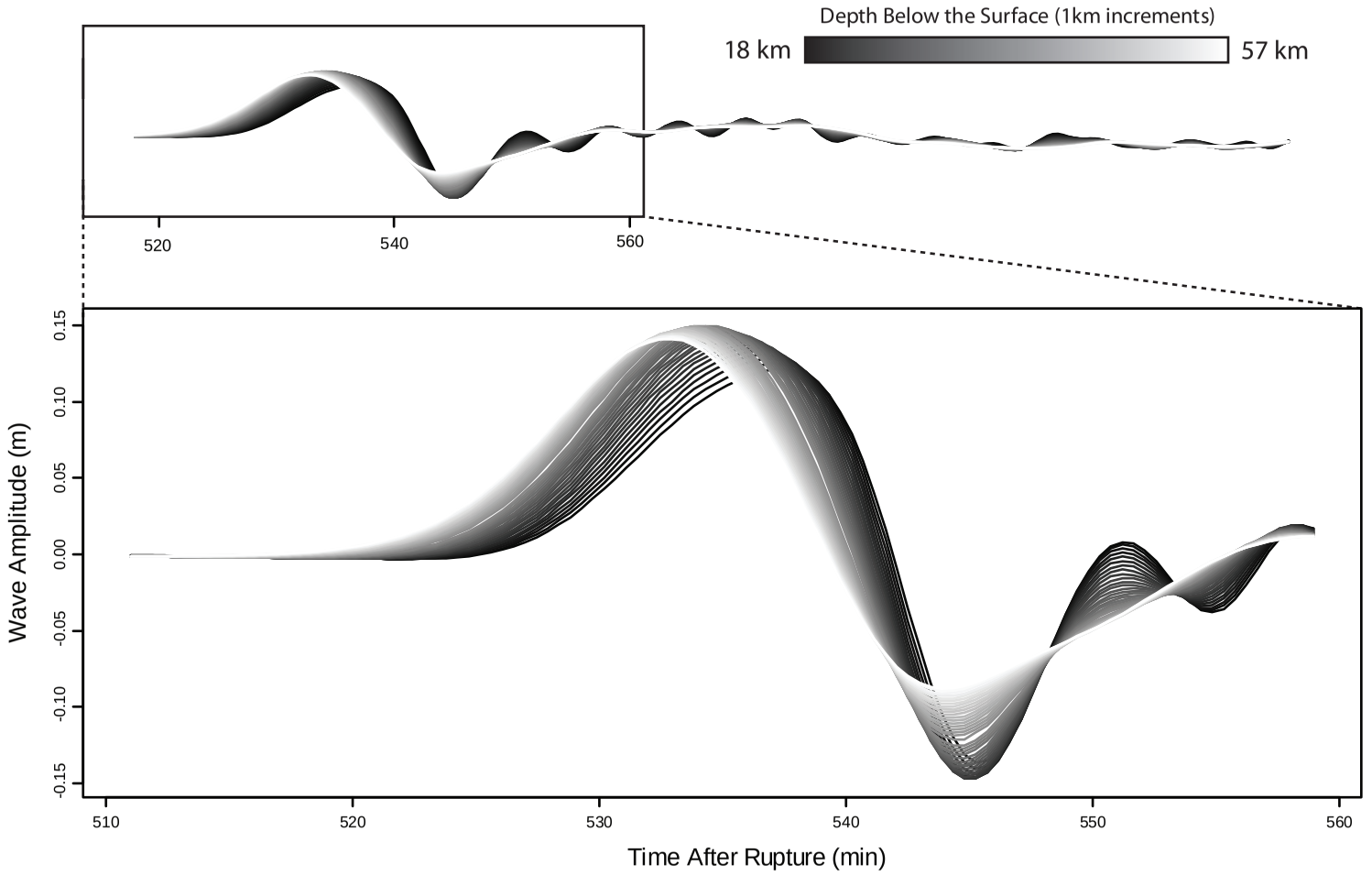

Figure 14. - Simulated time series data for dart buoy DMAR, illustrating the effect of earthquake depth on the resulting tsunami wave train. Each line represents a different simulation, with 40 in total. Earthquake parameters other than depth are held constant at the following values: Strike = 15°, Dip = 20°, Rake = 90°, M_W = 8.5, Latitude = 36° S, Longitude = 73° W.

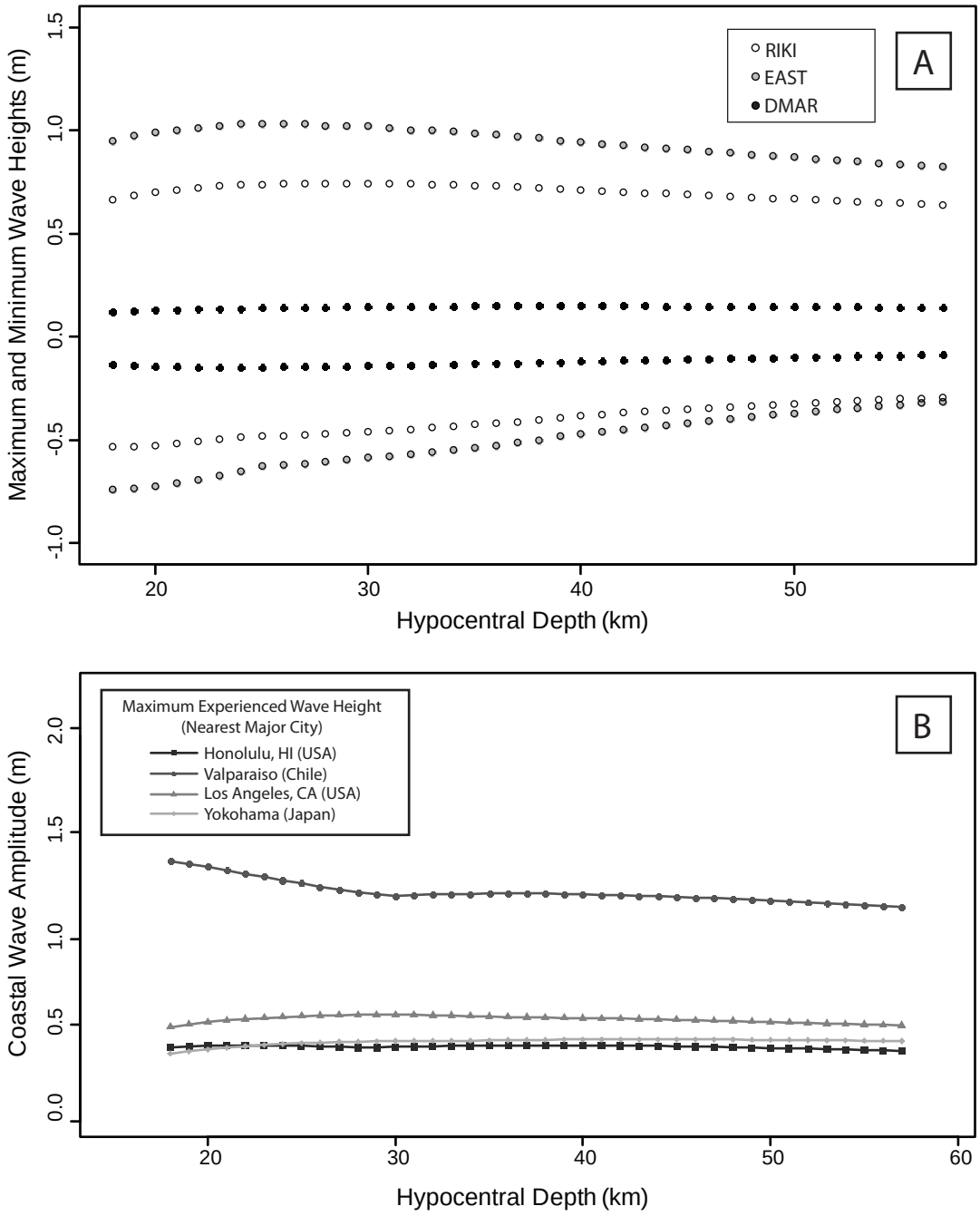

Figure 15. - Graph A illustrates maximum and minimum wave heights experienced at tide gauges EAST, RIKI, and DART buoy DMAR. Earthquake parameters other than depth are held constant at the following values: Strike = 15, Dip = 20°, Rake = 90°, M_W = 8.5, Latitude = 36° S , Longitude = 73° W. Graph B shows coastal wave height predictions with incremental changes in hypocentral depth. Coastal forecasts are generated using Green's Law.

forced to make assumptions about fault geometries, usually based on the tectonic environment near the hypocenter, when calculating coastal wave hazard. Therefore, it is important that modelers understand the possible effects of misspecifying initial conditions in their models. This study provides insight into the impact of misspecifying fault geometry and earthquake depths when modeling tsunamis in real-time.

Even though some of the earthquakes presented in this study may seem geologically implausible given the source location, they are included to make the results more broadly applicable. For non-subduction locations that have high tsunami generating potential, such as the Hawaiian Islands, it is difficult to anticipate the nature of the fault that will eventually rupture. As a result, it is necessary that a model be robust enough to accurately model any potential fault, not just those along a plate interface.

As stated previously, the parameters of the base earthquake in this study were chosen based on an average fault location and orientation of the décollement at the Nazca-South American plate boundary. Models like the one described in Titov et al. (2001a) assume that all tsunami generating earthquakes are shallow thrusts occurring on a plate boundary, and as a result can only model earthquakes with locations fixed to subduction zones. While faults generated in these stress regimes will on average orient themselves parallel to the trench, this does not mean that fault parameters cannot deviate from known plate boundary orientations.

The rest of this section will be focused on how coastal wave amplitude estimates change as fault orientation deviates from the décollement. Figure 16 summarizes wave height predictions for all four studied parameters. The data is plotted in a way that allows for easy comparison between the waves created by décollement slip

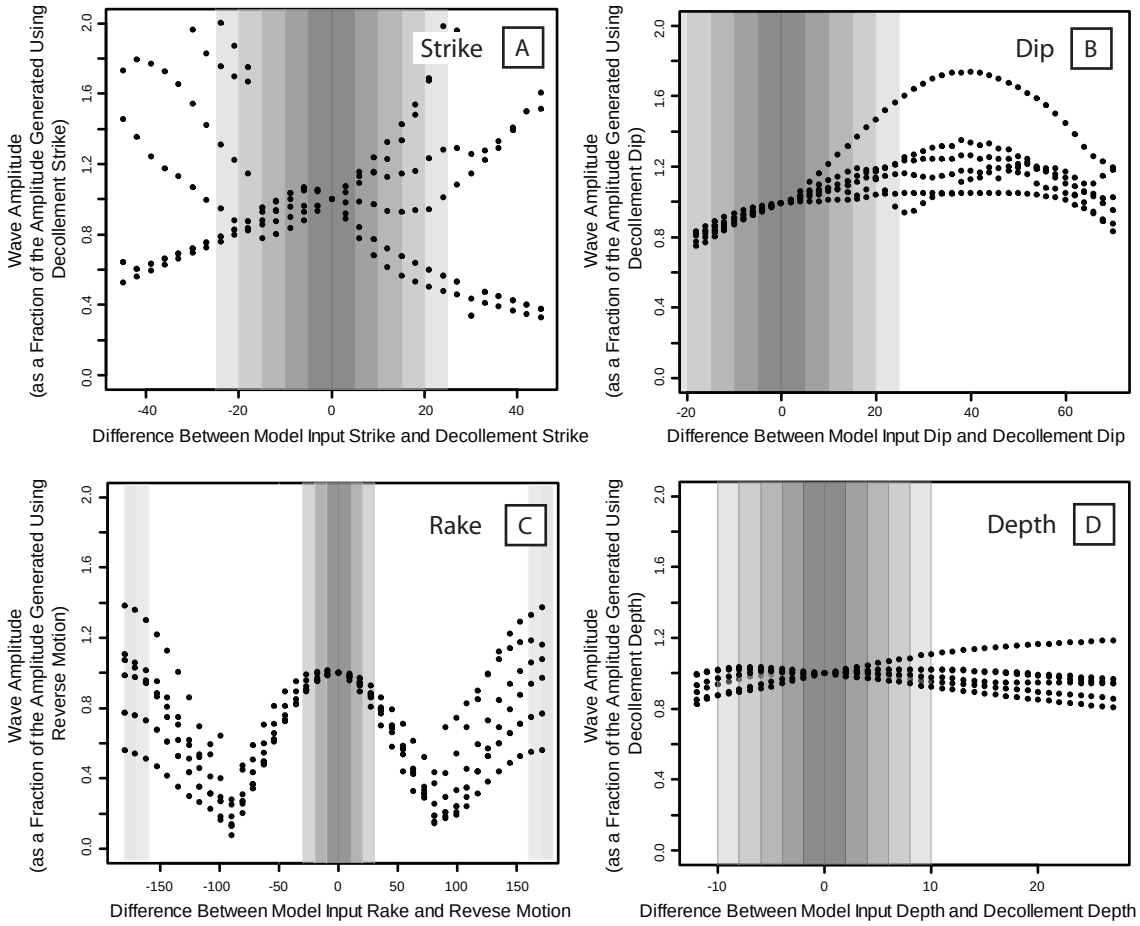

Wave Heights (%)

	Strike	Dip
Within 5°	± 10%	± 8%
Within 10°	± 20%	± 20%
Within 15°	± 40%	± 25%
Within 20°	± 90%	± 35%
Within 25°	± >100%	± 60%

	Rake
Within 10°	± 5%
Within 20°	± 10%
Within 30°	± 15%
Within 10° of Normal	± 50%
Within 20° of Normal	± 50%

	Depth
Within 2 km	± 3%
Within 4 km	± 8%
Within 6 km	± 12%
Within 8 km	± 13%
Within 10 km	± 15%

Figure 16. - Graphs showing normalized far-field wave heights for different fault orientations (measure relative to the Nazca/South American decollement). Plot A shows wave heights for varying strikes, with faults measured against an average decollement strike of 015°. Plot B indicates amplitude estimates as dip is varied, measured against a decollement dip of 20°. Plot C shows differences in wave amplitudes for various rake angles, centered around pure thrust motion. Finally, plot D indicates the impact of fault depth on wave heights, centered on an assumed decollement depth of 30 km. Highlighted in grey are incremental deviations from decollement fault orientation. The values in the tables below indicate % changes in wave height with each incremental step away from decollement fault orientation.

and those created by other fault orientations. The x-axis represents the difference between the parameter value used in a model run and décollement's parameter value. Therefore, wave heights generated by slip on the décollement plot at an x-value of 0. To compare wave heights from all 6 different far-field locations, the maximum amplitude at each location is normalized to 1 for décollement slip. As a result, a 0.01 change in the y-values on the graph correspond to a 1% deviation in wave height from the values predicted by décollement slip.

It is clear from the wave field analysis that fault strike has a strong control over the direction of tsunami energy propagation (Figure 3). The effect is hard to quantify based on the tsunami wave heights at individual locations (as evidenced by Figure 16A). Unlike the other parameters which seem to affect tsunami severity at all locations, strike causes large but local changes in predicted wave height. The beam of maximum amplitude trends perpendicular to fault strike, so as fault strike deviates from trench parallel, the locations with the greatest impending tsunami threat will change. This could present problems for hazard management, especially given that trench orientation in this region varies between 10° and 30°.

Gica (2007) found that there were only slight variations in the far-field wave heights for dip values within a reasonable range of décollement dip. He also found, however, that when dips approached 90° there was a 65% change in the experienced wave heights in the far-field. Unlike the results found in Gica's (2007) sensitivity study, the maximum difference in expected amplitude occurred at 60° with RIFT, and waves were approximately 80% larger than those an earthquake on the décollement would have

generated. Even with slight deviations (as little as 10°), the produced waves were 20% larger in some locations.

Fault rake directly controls tsunami wave height. Although there is only a 15% difference in maximum wave height when fault rake is within 30° of pure convergence, wave heights change significantly between normal and reverse motion. Estimates ranged from 30% higher to 50% lower when the motion on the fault was normal. Gica (2007) found that for values within 45° of 90°, the variation in far-field wave heights will not be significant. For rake angles near 30° and 150°, however, the wave heights fell as much as 50%. I also find that when the fault rake deviates by 60° from normal, wave heights fall by nearly 60%.

Over the range of values tested, hypocenter depth is the only parameter that seems to have a negligible effect on tsunami hazard. With a difference of 30 km from the décollement depth, there was at most a 20% difference in estimated wave height. Gica (2007) found that the effects of depth were location specific; for the subduction zones adjacent to Chile and Japan no effect could be seen as a result of varying hypocentral depth, however in the Aleutian Islands there was an appreciable change in wave height (34%) as depth varied within a reasonable range. This point presents an important caveat to the results presented in this study; the trends indicated may change with a different source location. Future study is required to determine which effects, if any, are location specific.

6. CONCLUSION

Historic tsunamis provide a baseline against which models can be tested, but limited historic data combined with an incomplete theoretical understanding of

tsunamigenesis makes it difficult to ever truly validate a model. This study is primarily an analysis of RIFT, a look at how a change in input parameters changes the resulting output. Even though historic validation of RIFT has shown that wave height predictions reflect observed historic wave heights, it is important that any extrapolation outside of a modeling context be done with caution. Having stated that, I believe this study makes it possible to better understand the impact of specific fault parameters on tsunamigenesis.

This study shows that fault orientation and location have profound implications for tsunami hazard calculations. While hypocentral depth does not significantly affect wave amplitude predictions, fault strike, dip, and rake can all bias hazard forecasts if inaccurate values are assumed. Models which do not have customizable source parameters introduce a large potential for error by restricting tsunami generating earthquakes to the décollement.

Tsunamigenesis is not restricted to the shallow thrust, plate interface earthquakes that some modelers assume. It is clear now that normal faulting, splay faults, and other non-décollement slip near subduction zones can create equally destructive tsunamis. For that reason, it is important that models do not focus merely on the most common tsunamigenic events, but instead are adaptable enough to model any potential tsunamigenic earthquake.

7. ACKNOWLEDGEMENTS

I would like to thank Gerard Fryer, Dailin Wang, and Nathan Becker of the Pacific Tsunami Warning Center for their help in working with RIFT and designing code to help visualize the results. I would also like to thank Sarah Titus for her help in formalizing the results, and the Carleton Geology department for their support throughout

my education in the geosciences. This research was performed under appointment to the National Oceanic and Atmospheric Administration's Ernest F. Hollings Undergraduate Scholarship, administered by Oak Ridge Associated Universities.

REFERENCES

Comer, R., 1984, Tsunami generation; a comparison of traditional and normal mode approaches: The Geophysical Journal of the Royal Astronomical Society, v. 77, p. 29-41.

Fryer, G., Holschuh, N., Becker, N., and Wang, D., 2010, Improving Tsunami Warning with a Rapid Linear Model, American Geophysical Union, Fall 2010: San Francisco, CA.

Gica, E., 2007, Sensitivity Analysis of Source Parameters for Earthquake-Generated Distant Tsunamis: Journal of Waterway, Port, Coastal, and Ocean Engineering, v. 133, p. 429-441.

Greenslade, D., 2008, A Comparison Study of Two Numerical Tsunami Forecasting Systems: Pure and Applied Geophysics, v. 165, p. 1991-2001.

Grilli, S. T., 2010, Numerical simulation and first-order hazard analysis of large co-seismic tsunamis generated in the Puerto Rico trench: Near-field impact on the North shore of Puerto Rico and far-field impact on the US East Coast: Natural Hazards and Earth System Sciences, v. 10, p. 2109-2125.

Helffrich, G. R., 1997, How good are routinely determined focal mechanisms? Empirical statistics based on a comparison of Harvard, USGS and ERI moment tensors: Geophysical Journal International, v. 131, p. 741.

Lima, V. V., 2010, Impact of a 1755-like tsunami in Huelva, Spain: Natural Hazards and Earth System Sciences, v. 10, p. 139-148.

Okada, Y., 1985, Surface deformation due to shear and tensile faults in a half-space: Bulletin of the Seismological Society of America, v. 75, p. 1135-1154.

Okal, E., 2009, Excitation of Tsunamis by Earthquakes, Tsunamis, Harvard University Press, p. 450.

Pasyanos, M. E., Dreger, D. S., and Romanowicz, B., 1996, Toward real-time estimation of regional moment tensors: Bulletin of the Seismological Society of America, v. 86, p. 1255-1269.

Synolakis, C. E., 1991, Green's Law and the Evolution of Solitary Waves: Physics of Fluids, v. 3, p. 490-491.

Synolakis, C. E., and Skjelbreia, J. E., 1993, Evolution of Maximum Amplitude of Solitary Waves on Plane Beaches: Journal of Waterway Port Coastal and Ocean Engineering-Asce, v. 119, p. 323-342.

Titov, V., Gonzalez, F., Mofjeld, H., and Newman, J., 2001a, Project SIFT (Short-term Inundation Forecasting for Tsunamis), *in* ITS.

Titov, V. V., Mofjeld, H. O., Gonzalez, F., and Newman, J. C., 2001b, Offshore forecasting of Alaska-Aleutian Subduction Zone tsunamis in Hawaii, Tsunami Research at the End of a Critical Decade: Birmingham, England, Kluwer Acad. Pub., p. 75-90.

Wang, D., Becker, N., Walsh, D., and Fryer, G., 2010, Tsunami Wave Propagation Forecast in Real Time: A Methodology and Applications, PTWC, p. 48.

Wang, X., 2005, A numerical investigation of Boumerdes-Zemmouri (Algeria) earthquake and tsunami: Computer Modeling in Engineering and Sciences, v. 10, p. 171-184.

Yeh, H., 2007, Effects of the 2004 Great Sumatra Tsunami: Southeast Indian Coast: Journal of waterway, port, coastal, and ocean engineering, v. 133, p. 382-400.